PNAS RESEARCH ARTICLE | APPLIED PHYSICAL SCIENCES

Nanoparticle-blockage-enabled rapid and reversible nanopore gating with tunable memory

Rami Yazbeck[a,1], Yixin Xu[a,1], Tyrone Porter[b], and Chuanhua Duan[a,2]

Edited by David Weitz, Harvard University, Cambridge, MA; received January 20, 2022; accepted May 15, 2022

Gated protein channels act as rapid, reversible, and fully-closeable nanoscale valves to gate chemical transport across the cell membrane. Replicating or outperforming such a high-performance gating and valving function in artificial solid-state nanopores is considered an important yet unsolved challenge. Here we report a bioinspired rapid and reversible nanopore gating strategy based on controlled nanoparticle blockage. By using rigid or soft nanoparticles, we respectively achieve a trapping blockage gating mode with volatile memory where gating is realized by electrokinetically trapped nanoparticles near the pore and contact blockage gating modes with nonvolatile memory where gating is realized by a nanoparticle physically blocking the pore. This gating strategy can respond to an external voltage stimulus (~200 mV) or pressure stimulus (~1 atm) with response time down to milliseconds. In particular, when 1,2-diphytanoyl-sn-glycero-3-phosphocholine liposomes are used as the nanoparticles, the gating efficiency, defined as the extent of nanopore closing compared to the opening state, can reach 100%. We investigate the mechanisms for this nanoparticle-blockage-enabled nanopore gating and use it to demonstrate repeatable controlled chemical releasing via single nanopores. Because of the exceptional spatial and temporal control offered by this nanopore gating strategy, we expect it to find applications for drug delivery, biotic–abiotic interfacing, and neuromorphic computing.

nanopore gating | gated protein channels | nanoparticle blockage | liposome | electrokinetic

Significance

One of the most original yet unachieved goals of nanofluidics is to completely replicate the gating function of biological protein channels in artificial nanoconduits. Despite tremendous efforts, rapid, complete, and reversible gating have not been simultaneously achieved in individual nanoconduits. Here, we report a novel nanoparticle-blockage-enabled nanopore gating strategy using either rigid or soft nanoparticles that can have either volatile or nonvolatile memory. We further show that excellent gating performance comparable with gated protein channels in every aspect can be achieved by using liposome via the reversible formation and breakdown of a liposome-rupture-induced lipid bilayer and use it to demonstrate controlled chemical releasing. This work represents significant progress in nanofluidics that holds great promise for cell communication and stimulation, precise drug delivery, and ionic-based computation and storage.

Living cells use specially designed nanopores such as voltage- or stretch-gated protein channels as gates or valves to control ion and molecular transport across the cell membrane (1–3). Benefiting from the unique molecular structures of these naturally occurring nanopores, reversible gating can be achieved with millisecond response time upon various small external stimuli, including voltages, pressure, temperature, and chemical concentration gradients (1, 4, 5). Replicating such gating functions in artificial solid-state nanopores has been a focus of modern nanofluidics over the last 20 years as gated solid-state nanopores hold great promise for numerical practical applications including sensing, drug delivery, signal transduction, and neuromorphic computing (6–9).

To date, a variety of nanopore gating strategies that rely on conformation change of surface grafted functional polymers (9–11), electrostatic interaction (7, 8, 12), or plasmonic effects (13–15) have been reported. Even though these strategies offer fast open/close response time in correspondence to electrical, mechanical, or optical stimuli, they still suffer from low gating efficiency (i.e., incomplete closing) and typically require much larger stimuli than gated protein channels. On the other hand, other types of nanopore gating strategies that take advantage of wetting-based transport barriers (e.g., bubbles or capillary-stabilized immiscible liquid) near or inside the nanopore have been developed (16–18). While these wetting-based strategies can achieve complete gating, they either exhibit slow switching time or poor repeatability while still requiring large stimuli (e.g., large voltages on the order of 1–10 V) or are difficult to use to control open/close of individual nanopores. Therefore, despite significant efforts, currently there are no nanopore gating strategies that have fully replicated the gating functions in protein channels by providing all together complete gating, fast switching time, and high reversibility on single nanopores with small external stimuli (19).

To improve the gating performance in artificial nanofluidic devices, it is necessary to further learn and exploit the gating mechanisms used by gated protein channels. One of the most well-known gating mechanisms in voltage-gated protein channels is the ball-and-chain inactivation mechanism (20, 21). In this mechanism, a ball of amino acids (which is the actual gate) is anchored by a string of residues (which is the chain) outside of the protein channels, and the ball can reversibly and completely block and unblock the protein channels within tens of milliseconds in response to ~100 mV action potentials. Although this ball-blockage-based gating mechanism provides excellent gating performance for voltage-gated protein channels, it has not been replicated

Author contributions: R.Y., Y.X., T.P., and C.D. designed research; R.Y., Y.X., and T.P. performed research; R.Y. and Y.X. analyzed data; and R.Y., Y.X., and C.D. wrote the paper.

The authors declare no competing interest.

This article is a PNAS Direct Submission.

[1]R.Y. and Y.X. contributed equally to this work.

[2]To whom correspondence may be addressed. Email: duan@bu.edu.

This article contains supporting information online at http://www.pnas.org/lookup/suppl/doi:10.1073/pnas.2200845119/-/DCSupplemental.

Published June 27, 2022.

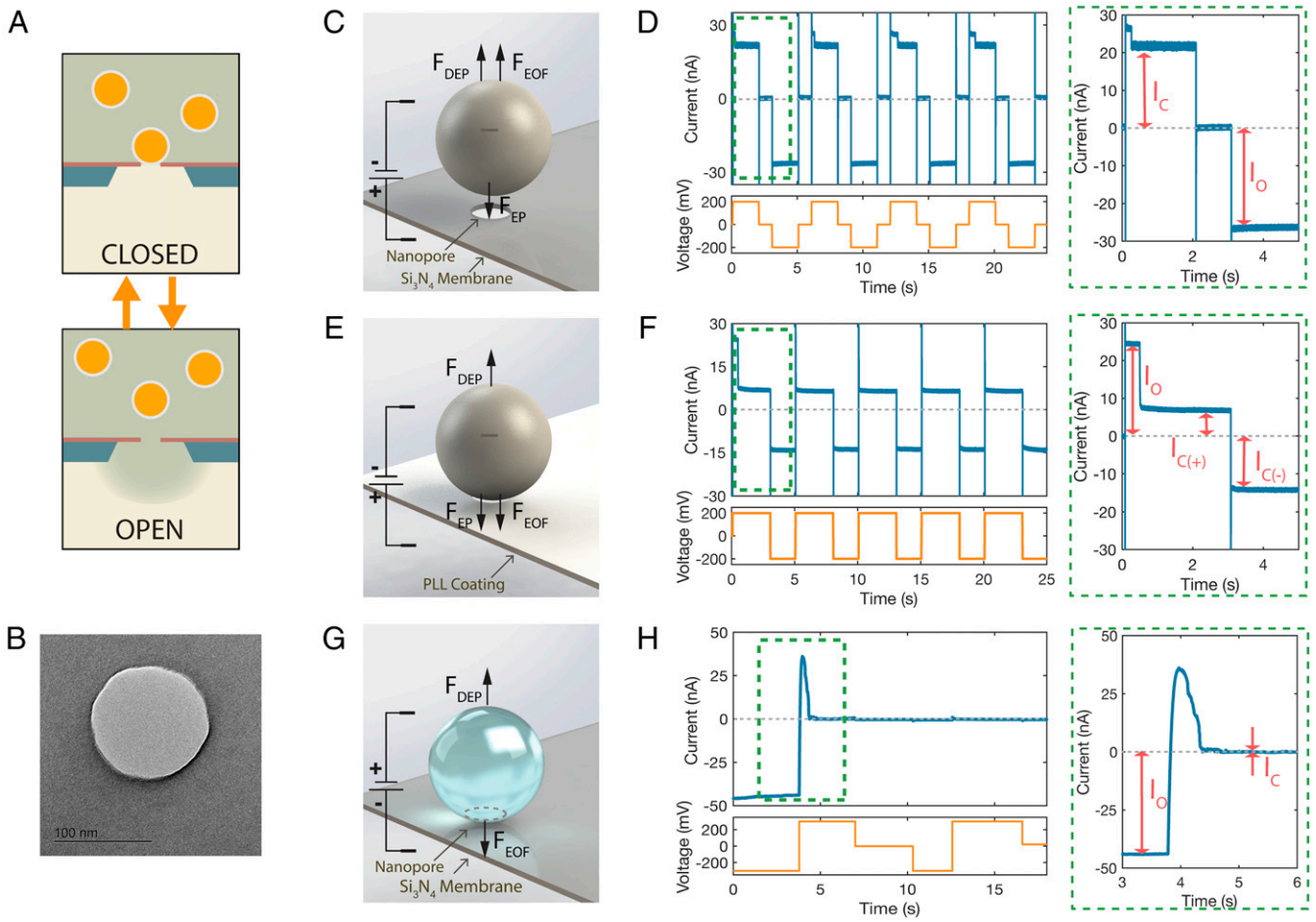

Fig. 1. Concept and experimental results of NBE gating strategy using various nanoparticles and electrical stimuli. (*A*) Schematic illustration of the general NBE gating strategy. The nanopore conformation is in the closed state when a nanoparticle is stuck at the pore entrance and obstructs the transport through the pore, while the pore is back to the open state when the nanoparticle is released. (*B*) TEM image of a typical silicon nitride nanopore used in the study. (*C*–*H*) Mechanism illustrations, ionic current signal traces (blue), and voltage stimuli (orange) of trapping (*C* and *D*), contact blockage (*E* and *F*), and LBE nanopore gating (*G* and *H*), where F_{EP}, F_{EOF}, and F_{DEP} refer to electrophoretic force, electroosmotic force, and dielectrophoretic force, respectively. The zoom-in current signals on the right in *D*, *F*, and *H* show the first cycle of each gating mode, where I_O and I_C refer to the current of the open and closed states, respectively. The gating experiments of rigid nanoparticles and liposomes were performed in 115- and 150-nm-diameter SiN nanopores, respectively. The nanopores used in the contact blockage gating were coated with an extra poly-l-lysine layer. The particles used in trapping and contact were PS-COOH with an average diameter of 390 nm, and the ones used in LBE were DPhPC liposomes with an average diameter of 327 nm.

in artificial nanofluidic systems. In contrast, blockage or clogging has always been considered as a failure for nanopore-involved applications (22, 23).

Herein, we demonstrate that we can use rigid/soft nanoparticles to achieve rapid and reversible nanopore blockage, which effectively gates the nanopore similar to the ball-and-chain mechanism found in nature with comparable time response and gating efficiency. Such nanoparticle-blockage-enabled (NBE) gating can be simply achieved by introducing nanoparticles with diameter larger than the nanopore on one side of the nanopore. The high nanoparticle concentration in solution and fast electrokinetic/hydrodynamic motion of the nanoparticles ensure rapid response under small electrical or mechanical stimuli (22, 24). We can further change the nanoparticle and nanopore interaction to tune the gating reversibility, the gating efficiency, and the memory for the open/closing state.

Results and Discussion

Trapping Blockage Mode. We first tried the NBE gating strategy in silicon nitride (SiN) nanopores by using charged rigid nanoparticles and electrical stimuli. The pore conformation is termed closed when a nanoparticle blocks the pore entrance, impeding transport through the nanopore, and open when there is no nanoparticle near the pore, as is illustrated in Fig. 1*A*. Fig. 1*B* is a transmission electron microscope (TEM) image of a typical SiN nanopore in our study. We have found that when a charged nanoparticle is electrokinetically driven toward a nanopore that has surface charges with the same polarity, the nanoparticle would not be physically in contact with the nanopore. Instead, it would be trapped in a position close to the nanopore due to a competition between electrophoretic force, electroosmotic drag force, and dielectrophoretic forces and partially block transport through the nanopore (see Fig. 1*C* and *SI Appendix*, section S1) (25, 26). The trapped nanoparticle can be quickly released by reversal of the applied bias. Thus, such a trapping-induced blockage phenomenon can result in a nanopore gating mode that can rapidly respond to electrical stimuli.

Fig. 1*D* shows a current trace displaying multiple open-and-close cycles under a capture voltage pulse of +200 mV, a release voltage pulse of –200 mV (both durations are 2 s), and a relax time (duration of 1 s, intermediating capture and release pulses) when using a carboxylated polystyrene nanoparticle (PS-COOH) solution with a concentration of 2.9×10^{10} particles/mL (48 pM), diameter of 390 ± 6.6 nm, and zeta potential of –42.5 ± 13.6 mV in a 115 ± 5 nm SiN nanopore. Shortly after the positive bias is

applied, a blockage event occurs (translocation current decreases from 27 to 22.5 nA), and the nanopore switches from the open state to the closed state. When the voltage is reversed, the current quickly reaches –27 nA and the nanopore returns to the open state, as the blocked nanoparticle is released. This trapping blockage gating is highly repeatable, and the nanopore opening/closing current does not change between cycles (see Fig. 1*D* and *SI Appendix*, section S2).

It is worth noting that once the corresponding voltage is removed, the trapped nanoparticle is released instantly and the nanopore status changes from the closed state back to the open state (see *SI Appendix*, section S3). Such memory characteristics are defined as volatile memory, which is widely observed in electronic volatile memory devices where all stored data are lost when power is removed. In fact the trapping-blockage gating mode shares several similarities with the basic memory cell of an electronic volatile memory device; both of them can store binary data 0 or 1 (for nanopore, 0 is stored when the pore is open and 1 is stored when the pore is blocked by the trapped nanoparticle), and the memory of state 1 is volatile (27–29). However, the nanoparticle-blocked nanopore at the trapping mode still cannot fully mimic an electronic volatile memory cell. The current nanopore system has only two electrical connections (one for ground and one for combined writing/reading), compared to three for the basic electronic volatile memory cell, including one for ground, one for the word line, and one for the bit line. Since the writing voltage is also the reading voltage for both the 0 and 1 state of the current nanopore system, it is impossible to use one specific reading voltage to read the two different states of the nanopore (30, 31). In order to fully replicate the functionality of the electronic volatile memory cell, another electrical connection (for writing) needs to be added to the system to control nanoparticles moving toward/away from the nanopore.

In addition to the volatile memory characteristics, the trapping blockage mode also exhibits short closing/opening response times. The closing response time (t_{closed}), which is the time it takes to switch from open to closed state after the stimulus is applied, is measured to be 0.1 s (CI 95% 0.12 s, 0.18 s) for a 2.9×10^{10} particles/mL solution. We have further discovered that t_{closed} is proportional to nanoparticle concentration and can be further lowered to the system capacitance response time (~2 ms) when higher concentrations are used (see *SI Appendix*, section S4). On the other hand, the opening response time (t_{open}), which is the response time to switch from the closed state to the open state, does not show concentration dependence and is always shorter than our system capacitance response time. Despite the rapid response, the gating efficiency, defined as $\frac{I_{open}-I_{closed}}{I_{open}}$, for the trapping blockage mode using this PS-COOH nanoparticle and SiN nanopore combination is only 17.9 ± 0.2%. This gating efficiency is obtained from more than 200 continuous trapping/releasing cycles per nanopore device (which accounts for the deviation of particle size/zeta potential since for each cycle a different nanoparticle is trapped) and from more than three different nanopore devices (which account for the pore size deviation) (see *SI Appendix*, section S2). Although we found that such gating efficiency can be further improved by increasing the particle size or surface charge density or decreasing the pore size, the gating efficiency is generally not higher than 40% for such a trapping blockage mode (25).

Contact Blockage Mode. To accomplish higher gating efficiency, it is necessary to either reduce or reverse the force generated by the electroosmotic flow from the nanopore such that nanoparticles no longer experience a force balance near the nanopore (see Fig. 1*E*) and thus physically block the nanopore when being electrokinetically driven toward the pore (25, 32). In such a case, the trapping blockage mode switches to a contact blockage mode. We found that such contact blockage gating mode shows very different gating behaviors compared with the trapping mode. Fig. 1*F* shows the current trace for the contact blockage gating mode in a 115-nm poly-l-lysine (PLL) coated SiN nanopore with 390-nm PS-COOH nanoparticles and ± 200-mV voltage pulses. PLL coating changed the surface charged density of the nanopore from –3.1 ± 0.03 mC/m^2 to +5.8 ± 2.1 mC/m^2 (see *SI Appendix*, section S5). Although the closing response time is similar to that of the trapping mode, it is clear that the gating efficiency becomes much higher (70.4 ± 2.7% in this case) than that of the trapping mode. Moreover, the gating becomes irreversible after the initial blockage, indicating permanent nonvolatile memory for the closed state (see Fig. 1*F* and *SI Appendix*, section S6). Applying a reverse voltage pulse would not release the nanoparticle, and the nanopore remains blocked with an apparently smaller gating efficiency of 38.9 ± 2.5%. We found that the smaller gating efficiency (larger current) occurring under the reverse bias is a result of current rectification instead of the change of nanoparticle physical position. The permanent presence of a nanoparticle at the entrance of the nanopore introduces a surface charge discontinuity and asymmetry in the pore geometry, resulting in a rectified, diode-like current behavior (33, 34). This rectification behavior is diminished when lower voltages (e.g., 25 mV) are applied. In that case, both the reverse and forward bias exhibit the true gating efficiency of 70.4 ± 2.7% (see *SI Appendix*, section S7). This gating efficiency is obtained from at least five different blockage events, each from a different nanopore device.

The irreversible gating and nonvolatile memory result from strong van der Waals interactions between the nanoparticle and the nanopore. While it may be useful for some applications like data storage and one-time-use valves, a higher gating efficiency would be more appealing (which means the closing state becomes more distinguishable). Such incomplete blockage is not dependent on the particle and pore size (see *SI Appendix*, section S8). We hypothesize that it results from the imperfect shape of the circular nanopore or the spherical nanoparticle or from an imperfect blockage position (the center of the nanopore may not be coaxial with the nanoparticle). Our simulation results show that a 4.7-nm misalignment would lead to significant leakage and a gating efficiency of 70% (see *SI Appendix*, section S9).

Liposome-Blockage-Enabled Gating Mode. To further improve gating efficiency, we used artificial soft nanoparticles, liposomes that can deform upon physical contact (35, 36). The typical Young's modulus of liposomes is less than 100 MPa, which makes them extremely soft compared to the PS-COOH nanoparticles (Young's modulus 3–3.5 GPa) (37–40). We found that liposome formed with a pure 1,2-diphytanoyl-sn-glycero-3-phosphocholine (DPhPC) lipid bilayer can completely eliminate the aforementioned leakage gap and achieve 100% gating efficiency. Such liposomes are neutrally charged and can be driven with electroosmotic force (EOF) toward the pore and physically block the pore (Fig. 1*G*). As shown in Fig. 1*H*, this liposome-blockage-enabled (LBE) gating mode shows 100% gating efficiency. The unique nonvolatile memory for the closing state was maintained as the current remained zero after switching back to open pulse. We also found that even a 700-mV open voltage was insufficient to switch the pore to the open state (see *SI Appendix*, section S10).

A more interesting and exciting finding about this LBE gating mode is that the blockage state can be reversed by application of external pressure across the nanopore. Consequently, a complete gating (open followed by fully closed) cycle can be achieved in solid-state nanopore via this LBE gating with electrical and pressure pulses (see Fig. 2*A*). Fig. 2*B* shows the current trace of such a gating cycle using 1.7-nM solution of DPhPC liposomes that have an average diameter of 327 nm with a 5-s voltage pulse of +300 mV and a 1-s pressure pulse of 1.5 atm. A –10 mV voltage that would not disturb liposome motion was used to monitor the pore status. Clearly, the nanopore was completely closed ($I = 0$ nA) during stages "i" and "ii," and the pore was immediately reopened after the pressure pulse was applied. Such LBE gating is also highly repeatable, and the nanopore reopening/closing current remains the same (see Fig. 2*C*). As in trapping blockage gating, we found that the LBE gating shows fast opening/closing response, with a constant $t_{open} = 1.2 \pm 0.2$ ms and a closing response time down to 0.3 s (CI 95% 0.2 s, 0.4 s) for 1.7 nM (Fig. 2 *B* and *C*).

It is worth noting that although the pore remains open, the reopening current through the nanopore after the pressure pulse becomes smaller than that during the pressure pulse (Fig. 2 *B* and *C*), which may be a result of pressure-induced motion of the liposomes. The reopening extent compared to the pore fully open state is 67.5 ± 1.2%. It is also noteworthy that both the open and closed states were maintained even after the corresponding stimulus was removed, suggesting that this LBE gating mode has nonvolatile memory for both the open and closed states. We have further demonstrated the nonvolatile memory by electrically monitoring the pore status (Fig. 2 *D* and *E*). The nanopore remains open or closed even when the voltage/pressure pulse is removed for hours.

Controlled Chemical Releasing. Our results show that the LBE nanopore gating mode essentially leads to a nanofluidic gate/valve with complete gating, ultrafast switching ratio, excellent repeatability, rapid response, and long retention time. While this type of nanofluidic gate/valve has great potential for ionic-based data storage and neuromorphic computing (41–43), a straightforward application is controlled chemical releasing via pure diffusion at the nanoscale, which to our knowledge has never been achieved (19, 44). To prove the feasibility and applicability of our approach, we demonstrate controlled chemical releasing through a single 150-nm SiN nanopore by using fluorescein sodium salt (MW 376.3 Da, excitation/emission 460/515 nm) as the molecular tracer and an inverted fluorescence microscope. As illustrated in Fig. 3*A*, the nanopore device was placed in a custom-made Teflon holder, which consisted of two separate solution chambers and was mounted on the microscope. We introduced the tracer into the top reservoir (*trans*) and controlled its transport to the bottom reservoir (*cis*) by LBE gating. The influx rate was measured by recording the total fluorescent intensity change in the field of view (FOV) of the microscope camera and correlating it to the total amount of dye in the *cis* reservoir as a function of time. We compared fluorescein flux through the nanopore between the open and closed state. A SiN membrane without a nanopore was used for control experiments. Our results show that fluorescein flux through the open nanopore led to a linear increase of fluorescence in the *cis* reservoir, indicating a constant releasing rate of 0.13 fMole/s. This flux rate quantitatively matches simulation results based on pure diffusion and bulk diffusivity (see Fig. 3*B* and *SI Appendix*, section S11). It is also worth noting that the flux rate was large enough for location-specific single cell stimulation and communication (19, 45). In contrast, the liposome-blocked nanopore behaved exactly as a membrane without nanopores, which showed no diffusion of fluorescein into the *cis* reservoir over 1 h (see inset of Fig. 3*B*).

We also successfully demonstrated multicycle-controlled fluorescein flux through a single nanopore. Fig. 3*C* shows the changes of the amount of dye within the FOV during a multicycle

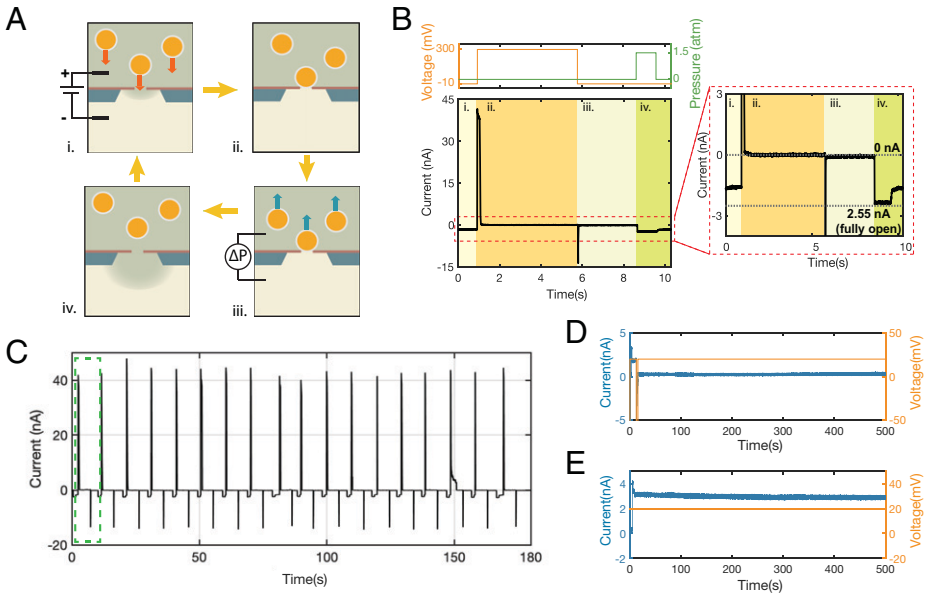

Fig. 2. LBE nanopore gating cycle. (*A*) Schematics illustrating the four stages of a complete LBE gating cycle. The nanopore is closed when the voltage stimuli drive the liposome nanoparticles toward the nanopore (i), and the nanopore is reopened when the pressure stimuli push the liposomes away from the pore (iii). △P stands for pressure difference between two reservoirs. (*B*) Voltage/pressure stimuli and the ionic current signal trace of one LBE gating cycle. The four sections correspond to the four stages illustrated in (*A*). The zoom-in current trace on the right illustrates the pore's open extent under –10-mV monitoring voltage. (*C*) Signal trace of the ionic current for 18 continuous cycles of the LBE gating. The green box represents the single LBE gating cycle shown in (*B*). (*D*) Current and voltage trace showing the nonvolatile memory of the closing state. With +20-mV monitoring voltage after the closing pulse, the current across the system remains around 0 nA, indicating the nanopore remained closed after the closing pulse. (*E*) Current and pressure trace showing the nonvolatile memory of the open state. A +20-mV monitoring voltage was applied to the system during the experiment, and the current remained around 3 nA after the opening pulse. This shows that the nanopore keeps open after the opening pulse. All experimental results were collected from 150-nm SiN nanopores with DPhPC liposomes with an average diameter of 327 nm.

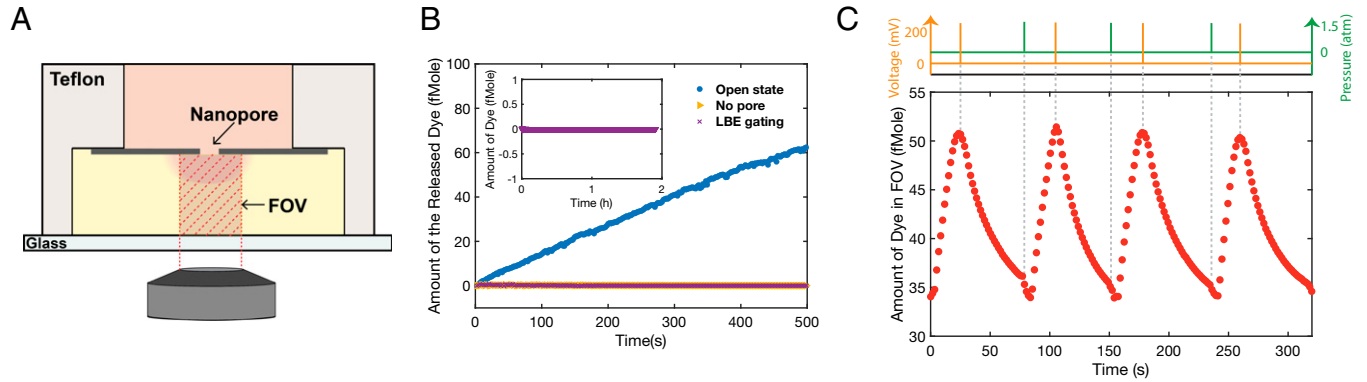

Fig. 3. Controlled fluorescein releasing from single nanopore. (*A*) Schematic illustration of the experimental setup. Fluorescein was introduced to the top reservoir and released to the bottom through the nanopore. An inverted microscope then was used to detect the dye within the FOV of the camera in the bottom reservoir. (*B*) Total amount of dye released to the bottom reservoir through the SiN membrane with a 150-nm open nanopore, no pore, and LBE gated nanopore. The total amount of dye was determined from the measured dye intensity within the FOV (see *SI Appendix*, section S11). An influx of dye was not detected when the pore was closed by LBE gating, proving the liposome nanoparticle can completely stop the transport of chemicals though the pore. (*C*) Results for multicycle LBE-gating-controlled fluorescein releasing from a single 150-nm nanopore with the corresponding applied stimuli. Liposomes with an average diameter of 327 nm were used to gate the pore. The amount of dye within the FOV responds quickly to the opening (pressure) and closing (voltage) stimuli.

releasing experiment (also see *SI Appendix*, section S12 for additional consecutive releasing cycles). We can clearly see that the fluorescence signal rapidly corresponds to the opening/closing pulse in each cycle. After the opening voltage pulse, the dye intensity continuously increased in the *cis* reservoir until the closing pulse was applied, after which the amount of dye in the FOV started to decrease because diffusion-based flux through the nanopore was negated and dye in FOV diffused out.

LBE Gating Mechanism. Having established a robust LBE nanopore gating system, we explored the underlying mechanism. First, we confirmed that the nanopore blockage was indeed a result of liposome motion under the applied electric pulse. Fig. 4*A* shows the scaning electron microscope (SEM) image of a liposome-blocked nanopore device that has drilled pores both inside and outside the SiN membrane. We were able to observe liposome covering only the pores inside the membrane but not those outside the membrane, which basically were not through pores and thus would not experience any electric field applied to the device (22) (also see *SI Appendix*, Fig. S13*A*).

We then used fluorescent DPhPC liposomes (i.e., liposome encapsulated dye solution) to check whether the complete blockage was a result of liposome deformation or rupture. In the latter case, a ruptured liposome can cover a nanopore with a lipid bilayer, otherwise known as a black lipid membrane (BLM) (46, 47). These fluorescent liposomes were tested in a chip that has a 10 × 10 array of 150-nm nanopores (see *SI Appendix*, Fig. S13*B*). After more than 95 of the nanopores were blocked by liposomes (which was confirmed by current-voltage (I-V) measurements and bright field microscope image; see *SI Appendix*, Fig. S13 *C* and *D*), we were not able to observe the fluorescent liposomes blocking the nanopores with the inverted microscope, although they were clearly recognizable outside of the membrane (Fig. 4*B*). On the other hand, we were able to spot fluorescent PS-COOH nanoparticles blocking the nanopores (see *SI Appendix*, Fig. S13*E*).

These experiments suggest that liposomes rupture upon contact with the nanopore, and the resulting BLM formation is probably the underlying mechanism for nanopore blockage. This mechanism will provide a method to prepare stable BLMs and protein channels in BLMs (either during liposome fusion or by later insertion) in solid-state nanopores. As the currently used techniques for BLM formation such as painting, direct fusion, and osmotic stress driven methods, either have a long-lasting stability/noise issue or have a significant degree of randomness (47–49). This method can overcome all these problems and revolutionize BLM-based electrophysiological approaches for evaluating physical properties and characteristics of protein channels. Consequently, the reopening of the nanopore by the pressure pulse would result from the partial but permanent breakdown of BLM. The reclosing would be achieved when a new liposome is electrokinetically driven toward the pore and fuses with the broken lipid bilayer to form a new BLM (Fig. 4*C*). This mechanism is supported by a previous study showing that pure DPhPC liposome adsorbs on a SiN surface tend to spread and spontaneously ruptures to form bilayer lipid membrane (49, 50). We have also used atomic force microscope (AFM) to examine the nanopore after achieving LBE gating and confirmed the presence of a single lipid bilayer spanning across the nanopore (see *SI Appendix*, section S14).

Such a rupture-based reversible gating mechanism was further supported by our study on the reclosing response time and reopening current after multicycle gating. We found that a higher liposome concentration led to a shorter reclosing response time (Fig. 4*D*), which confirms that reclosing relies on liposome in solution, and the broken BLM cannot reseal itself under the applied voltage pulse. We also noticed that, as shown in Fig. 2*C*, the extent of the reopening current did not decrease as more cycles were applied. Such an unchanged reopening current suggests that the thickness of the lipid membrane on top of the nanopore does not increase after multicycle gating, further confirming that the newly ruptured liposome would fuse into the broken BLM instead of forming another layer on top of it.

Conclusion

In summary, we have developed a NBE gating strategy that can rapidly and reversibly open and close solid-state nanopores in correspondence to electrical or mechanical pulses. Depending on the nanoparticles used in this strategy, either trapping blockage or contact blockage gating modes, which have varied gating efficiency and types of memory (volatile vs. nonvolatile), can be achieved. In particular, when DPhPC liposomes are used as the nanoparticles, we successfully achieved rapid, reversible, and complete gating with permanent nonvolatile memory, consequently realizing a high-performance nanofluidic valve. This liposome-induced contact blockage gating was found to result from a liposome-rupture-induced black lipid layer and its breakdown (or reforming) under a short electrical (or mechanical) pulse. We

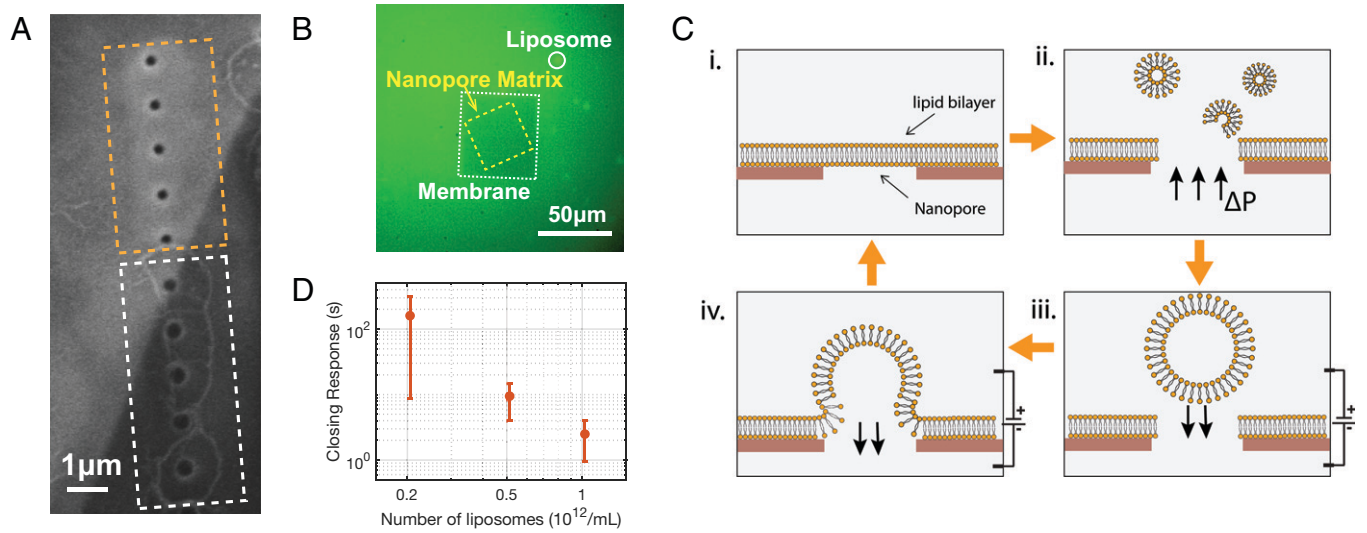

Fig. 4. Exploring the mechanism of LBE gating. (*A*) Scaning electron microscope (SEM) image of a nanopore device after the LBE gating experiment, where only the nanopores inside the SiN membrane (in white box) were covered with lipids while those outside the membrane (in yellow box) were not covered. (*B*) Microscopic image of a nanopore blocked by a fluorescent liposome. No fluorescent liposome was detected within the membrane (in white box), which indicates the liposome had already ruptured into the lipid bilayers. (*C*) Schematic illustrations of the hypothesized nanopore gating scenario during the LBE gating cycles. (*D*) Closing response of LBE gating with respect to various liposome concentrations. All the experiments were conducted with a 150-nm SiN nanopore with 327-nm DPhPC liposomes.

expect that the NBE gating strategy and the resulting two gating modes can find important applications in abiotic–biotic interfaces, drug delivery, and ionic-based computation and storage. We also believe that electrokinetics-induced liposome rupture on nanopores could be a simple way to create a stable BLM on solid-state nanopores to study protein channels and artificial porins.

Materials and Methods

Materials. Carboxylate-modified, monodispersed polystyrene particles (PS-COOH) with a mean diameter of 390 nm and stock concentration of 2.9×10^{12} particles/mL were purchased from Bangs Laboratories, Inc. (Fishers, IN). DPhPC liposomes were purchased from Avanti Polar Lipids, Inc. (Alabaster, AL). Phosphate-buffered saline (PBS) 10× concentrate, poly-L-lysine hydrobromide, fluorescein sodium salt, and all other reagents and solvents were purchased from Sigma-Aldrich (St. Louis, MO). Milli-Q filtered water (resistivity >18 MΩ.cm) was used for solution preparation and studies.

Nanopore Fabrication. The nanopore devices were 5- × 5-mm^2 silicon chips with a 50-nm-thick free-standing SiN membrane at the center. The free-standing membrane was fabricated via standard photolithography and etching techniques. A nanopore was drilled through the membrane with a focused gallium ion beam (FEI Quanta 3D FEG FIB) operated at 30 kV. A 2-μm-thick silicon dioxide layer sandwiched between the silicon substrate and the SiN layer was used to weaken the capacitive noise in the measured electrical current signal.

Electrical Measurement and Experimental Setup. Before each experiment, nanopore devices were cleaned with hot piranha solution (sulfuric acid/hydrogen peroxide, 3:1), rinsed with a stream of deionized water water and then dried with nitrogen. For the rigid nanoparticle contact mode experiment, the nanopore devices were placed for 12 h in a 0.1-mg/mL poly-l-lysine solution at room temperature, after which they were gently dried with nitrogen. After cleaning or surface modification, the chips were mounted in a custom Polytetrafluoroethylene (PTFE) cell, and a fast-curing silicone elastomer was used to seal the edges. The fluidic cell is composed of two chambers (*cis* and *trans*) that are connected only through the nanopore. Both chambers were filled with 1× PBS equivalent to 137 mM NaCl, 10 mM phosphate, and 2.7 mM KCl at pH 7.4. A silver/silver chloride electrode was inserted in each chamber, and the two electrodes were used to apply voltage across the nanopore and to collect the ionic current. The nanoparticles were introduced in the *cis*-chamber, which was at voltage ground. To reduce the effect of white noise, the entire fluidic cell was placed in a Faraday cage.

For the blockage experiments of rigid nanoparticles, current recordings were performed with an Axon 200B patch-clamp amplifier (Molecular Devices, Inc., Sunnyvale, CA) in the whole-cell mode with a CV-203BU head-stage. Data were acquired with a Digidata 1500 digitizer (Molecular Devices, Inc.) controlled by the Clampex 10.7. software (Molecular Devices, Inc.). Current recordings were performed at a sampling rate of 100 kHz, filtered with a low-pass filter at a cutoff frequency of 100 kHz, and analyzed in MATLAB R2019.

For the blockage experiments of soft nanoparticles, current recordings were performed with an eOne(b) amplifier (Elements SRL, Cesena (FC), Italy). Data were acquired with Elements Data Reader software (Elements SRL) at a sampling rate of 1.25–10 kHz and analyzed in MATLAB R2019.

Liposome Preparation. DPhPC liposomes were prepared by the standard extrusion method. A solution of 2 mg/mL DPhPC in chloroform (1 mL) was added to a round flask. The chloroform was evaporated with a dry stream of nitrogen, yielding a thin lipid film at the bottom of the flask. The lipid film was further dried by placing the flask in a vacuum chamber for >8 h. Afterward, 1× PBS solution (1 mL) was added to the flask, and the solution was allowed to hydrate at a temperature of 65 °C under vigorous stirring with a magnetic spin bar for 2 h. The product of hydration is large, multilamellar vesicles. The large vesicles were then extruded through polycarbonate filter membrane with 400-nm-diameter pores with a custom-made extrusion device (Mini-Extruder, Avanti Polar Lipids), forming small unilamellar vesicles referred to as liposomes. The liposome solution was stored at 4 °C and used within 5 d. Fluorescent DPhPC liposomes were prepared via a similar method with two different steps. First, instead of 1× PBs solution, 2.7 mM fluorescein sodium salt in 1× PBS was used to rehydrate the lipid film. Second, extra fluorescein in the solution (not encapsulated in the liposome) was removed by dialysis with dialysis tubing cellulose membranes (Sigma-Aldrich, 8–10 kDA cutoff).

Nanoparticle Characterization. In order to acquire information on the size and zeta potential (related to surface charge density) of the nanoparticles used in this study, we respectively performed dynamic light scattering measurement (DLS) and electrophoretic light scattering (ELS) by using NanoBrook Omni from Brookhaven Instruments. The DLS method measures the hydrodynamic Stokes–Einstein radius of particles undergoing Brownian motion by light scattering generated by an incident laser light source. The ELS method measures the movement of nanoparticles (electrophoretic mobility) under an applied electric field by laser Doppler velocimetry (frequency shift of an incident laser beam). The recorded frequency shifts are proportional to the speed of the particles and are used to measure the electrophoretic mobility and zeta potential. The rigid PS-COOH particle size was measured to be 390 ± 6.6 nm, and their

corresponding zeta potential was measured to be –42.5 ± 13.6 mV. The DPhPC liposome size was measured to be 327 ± 35.7 nm. Because of the low zeta potential of these liposomes, accurate measurement of their zeta potential is not available. Both DLS and ELS measurements were done by diluting 100 μL of ~1×10^{11} particles/mL solution in 2.6 mL of 1× PBS (equivalent to 137 mM NaCl, 10 mM phosphate, and 2.7 mM KCl at pH 7.4), then transferred to a plastic cuvette. In addition, all measurements were performed at room temperature. In the text we refer to the nanoparticles by their average diameter/zeta potential, which in each case is the result of more than 10 collected measurements.

Fluorescence Measurements. Fluorescein quantification was done with an IX-81 Olympus inverted fluorescent microscope (Olympus America, Center Valley, PA) equipped with a GFP (green fluorescent protein) filter cube (excitation 450–486 nm, emission 505–544 nm) and a Lumen 200-W illumination bulb. All measurements were done with a 40× objective lens (numerical aperture 0.6 and field of view 330 × 330 μm^2). Sixteen-bit images were acquired with a sCMOS ORCA-Flash 4.0 LT PLUS camera (Hamamatsu Photonics, Shizuoaka Pref., Japan) controlled by image acquisition software CellSens Dimension (Olympus). Images were acquired in time-lapse format in order to reduce the effect of photo bleaching while maximizing the signal/noise ratio. Images were analyzed for fluorescence intensity in ImageJ/FIJI software (National Institutes of Health). To account for background noise, we subtracted all acquired images by the first captured image after introducing the dye onto the reservoir (for more information about image processing and analysis, see *SI Appendix*, section S10).

Pressure Setup. The external pressure was provided by compressed air through an analog circuit card pressure transducer (Type 3110 Pressure Transducer, Marsh Bellofram). We programmed the transducer by using LabView to control and monitor the pressure output precisely. The pressure outlet was sealed to the *cis* chamber together with an Ag/AgCl electrode through a wye connector in order to ensure that the pressure and electrical field could be applied simultaneously without leakage.

Data Availability. All study data are included in the article and/or *SI Appendix*.

ACKNOWLEDGMENTS. This work was supported by the DARPA Young Faculty Award Program (no. D18AP00048). The authors thank the Photonics Center at Boston University for the use of their fabrication and characterization facilities. C.D. and R.Y. acknowledge the Boston University Nanotechnology Innovation Center for R.Y.'s Cross-Disciplinary Fellowship. The authors are also grateful for Siang Xiao's help with atomic force microscope characterization and for Chu-Yao Chou's assistance with device fabrication during the COVID-19 pandemic. And finally, special thanks to Angel Rubio, Chenguang Peng, and Joanna Chiu from Porter's lab for their assistance with liposome preparation and to Mohammad Amin Alibakhshi for continued collaboration in nanofluidics.

Author affiliations: [a]Department of Mechanical Engineering, Boston University, Boston, MA 02215; and [b]Department of Biomedical Engineering, University of Texas at Austin, TX 78712

1. W. A. Catterall, From ionic currents to molecular mechanisms: The structure and function of voltage-gated sodium channels. *Neuron* **26**, 13–25 (2000).
2. B. Martinac, Mechanosensitive ion channels: Molecules of mechanotransduction. *J. Cell Sci.* **117**, 2449–2460 (2004).
3. A. J. Yool, E. M. Campbell, Structure, function and translational relevance of aquaporin dual water and ion channels. *Mol. Aspects Med.* **33**, 553–561 (2012).
4. D. A. Doyle *et al.*, The structure of the potassium channel: Molecular basis of K+ conduction and selectivity. *Science* **280**, 69–77 (1998).
5. T. Heimburg, Lipid ion channels. *Biophys. Chem.* **150**, 2–22 (2010).
6. L. Bocquet, Nanofluidics coming of age. *Nat. Mater.* **19**, 254–256 (2020).
7. W. Guan, S. X. Li, M. A. Reed, Voltage gated ion and molecule transport in engineered nanochannels: Theory, fabrication and applications. *Nanotechnology* **25**, 122001 (2014).
8. Z. S. Siwy, S. Howorka, Engineered voltage-responsive nanopores. *Chem. Soc. Rev.* **39**, 1115–1132 (2010).
9. S. W. Kowalczyk, T. R. Blosser, C. Dekker, Biomimetic nanopores: Learning from and about nature. *Trends Biotechnol.* **29**, 607–614 (2011).
10. X. Hou, W. Guo, L. Jiang, Biomimetic smart nanopores and nanochannels. *Chem. Soc. Rev.* **40**, 2385–2401 (2011).
11. R. Y. Lim, J. Deng, Interaction forces and reversible collapse of a polymer brush-gated nanopore. *ACS Nano* **3**, 2911–2918 (2009).
12. R. Karnik *et al.*, Electrostatic control of ions and molecules in nanofluidic transistors. *Nano Lett.* **5**, 943–948 (2005).
13. Y. Li *et al.*, Photoresistance switching of plasmonic nanopores. *Nano Lett.* **15**, 776–782 (2015).
14. O. N. Assad *et al.*, Light-enhancing plasmonic-nanopore biosensor for superior single-molecule detection. *Adv. Mater.* **29**, (2017).
15. J. Croissant, J. I. Zink, Nanovalve-controlled cargo release activated by plasmonic heating. *J. Am. Chem. Soc.* **134**, 7628–7631 (2012).
16. M. R. Powell, L. Cleary, M. Davenport, K. J. Shea, Z. S. Siwy, Electric-field-induced wetting and dewetting in single hydrophobic nanopores. *Nat. Nanotechnol.* **6**, 798–802 (2011).
17. L. Cantley *et al.*, Voltage gated inter-cation selective ion channels from graphene nanopores. *Nanoscale* **11**, 9856–9861 (2019).
18. X. Hou, Y. Hu, A. Grinthal, M. Khan, J. Aizenberg, Liquid-based gating mechanism with tunable multiphase selectivity and antifouling behaviour. *Nature* **519**, 70–73 (2015).
19. P. D. Jones, M. Stelzle, Can nanofluidic chemical release enable fast, high resolution neurotransmitter-based neurostimulation? *Front Neurosci-Switz* **10**, 138 (2016).
20. C. Fan *et al.*, Ball-and-chain inactivation in a calcium-gated potassium channel. *Nature* **580**, 288–293 (2020).
21. T. Hoshi, W. N. Zagotta, R. W. Aldrich, Biophysical and molecular mechanisms of Shaker potassium channel inactivation. *Science* **250**, 533–538 (1990).
22. M. Davenport *et al.*, The role of pore geometry in single nanoparticle detection. *ACS Nano* **6**, 8366–8380 (2012).
23. E. Beamish, H. Kwok, V. Tabard-Cossa, M. Godin, Precise control of the size and noise of solid-state nanopores using high electric fields. *Nanotechnology* **23**, 405301 (2012).
24. W. N. Zagotta, T. Hoshi, R. W. Aldrich, Restoration of inactivation in mutants of Shaker potassium channels by a peptide derived from ShB. *Science* **250**, 568–571 (1990).
25. R. Yazbeck, M. A. Alibakhshi, J. Von Schoppe, K. L. Ekinci, C. Duan, Characterization and manipulation of single nanoparticles using a nanopore-based electrokinetic tweezer. *Nanoscale* **11**, 22924–22931 (2019).
26. L. Esfandiari *et al.*, PCR-independent detection of bacterial species-specific 16S rRNA at 10 fM by a pore-blockage sensor. *Biosensors (Basel)* **6**, E37 (2016).
27. V. Gupta, S. Kapur, S. Saurabh, A. Grover, Resistive random access memory: A review of device challenges. *IETE Tech. Rev.* **37**, 377–390 (2020).
28. C. Ye *et al.*, Physical mechanism and performance factors of metal oxide based resistive switching memory: A review. *J. Mater. Sci. Technol.* **32**, 1–11 (2016).
29. Y. T. Li *et al.*, An overview of resistive random access memory devices. *Chin. Sci. Bull.* **56**, 3072–3078 (2011).
30. Y. Nakagome, M. Horiguchi, T. Kawahara, K. Itoh, Review and future prospects of low-voltage RAM circuits. *IBM J. Res. Develop.* **47**, 525–552 (2003).
31. J. A. Mandelman *et al.*, Challenges and future directions for the scaling of dynamic random-access memory (DRAM). *IBM J. Res. Develop.* **46**, 187–212 (2002).
32. M. Firnkes, D. Pedone, J. Knezevic, M. Döblinger, U. Rant, Electrically facilitated translocations of proteins through silicon nitride nanopores: Conjoint and competitive action of diffusion, electrophoresis, and electroosmosis. *Nano Lett.* **10**, 2162–2167 (2010).
33. R. Karnik, C. Duan, K. Castelino, H. Daiguji, A. Majumdar, Rectification of ionic current in a nanofluidic diode. *Nano Lett.* **7**, 547–551 (2007).
34. M. A. Alibakhshi, B. Liu, Z. Xu, C. Duan, Geometrical control of ionic current rectification in a configurable nanofluidic diode. *Biomicrofluidics* **10**, 054102 (2016).
35. M. D. Mager, N. A. Melosh, Nanopore-spanning lipid bilayers for controlled chemical release. *Adv. Mater.* **20**, 4423–4427 (2008).
36. I. Reviakine, M. Gallego, D. Johannsmann, E. Tellechea, Adsorbed liposome deformation studied with quartz crystal microbalance. *J. Chem. Phys.* **136**, 084702 (2012).
37. S. Li, F. Eghiaian, C. Sieben, A. Herrmann, I. A. T. Schaap, Bending and puncturing the influenza lipid envelope. *Biophys. J.* **100**, 637–645 (2011).
38. A. Darvish *et al.*, Nanoparticle mechanics: Deformation detection via nanopore resistive pulse sensing. *Nanoscale* **8**, 14420–14431 (2016).
39. A. Morshed, B. I. Karawdeniya, Y. M. N. D. Y. Bandara, M. J. Kim, P. Dutta, Mechanical characterization of vesicles and cells: A review. *Electrophoresis* **41**, 449–470 (2020).
40. X. Liang, G. Mao, K. Y. S. Ng, Mechanical properties and stability measurement of cholesterol-containing liposome on mica by atomic force microscopy. *J. Colloid Interface Sci.* **278**, 53–62 (2004).
41. D. B. Strukov, G. S. Snider, D. R. Stewart, R. S. Williams, The missing memristor found. *Nature* **453**, 80–83 (2008).
42. G. Sun, Z. Slouka, H. C. Chang, Fluidic-based ion memristors and ionic latches. *Small* **11**, 5206–5213 (2015).
43. Y. B. Li, Z. R. Wang, R. Midya, Q. F. Xia, J. J. Yang, Review of memristor devices in neuromorphic computing: Materials sciences and device challenges. *J. Phys. D Appl. Phys.* **51**, (2018).
44. J. K. Patra *et al.*, Nano based drug delivery systems: Recent developments and future prospects. *J. Nanobiotechnol.* **16,** 1–33 (2018).
45. P. S. Kaeser, W. G. Regehr, Molecular mechanisms for synchronous, asynchronous, and spontaneous neurotransmitter release. *Annu. Rev. Physiol.* **76**, 333–363 (2014).
46. K. Kumar *et al.*, Formation of nanopore-spanning lipid bilayers through liposome fusion. *Langmuir* **27**, 10920–10928 (2011).
47. S. Rebaud, O. Maniti, A. P. Girard-Egrot, Tethered bilayer lipid membranes (tBLMs): Interest and applications for biological membrane investigations. *Biochimie* **107** (Pt A), 135–142 (2014).
48. R. H. Tunuguntla *et al.*, Enhanced water permeability and tunable ion selectivity in subnanometer carbon nanotube porins. *Science* **357**, 792–796 (2017).
49. S. Kresak, T. Hianik, R. L. C. Naumann, Giga-seal solvent-free bilayer lipid membranes: From single nanopores to nanopore arrays. *Soft Matter* **5**, 4021–4032 (2009).
50. M. Kocun, T. D. Lazzara, C. Steinem, A. Janshoff, Preparation of solvent-free, pore-spanning lipid bilayers: Modeling the low tension of plasma membranes. *Langmuir* **27**, 7672–7680 (2011).